

On the detection of shocks in the solar granulation

S.K. Solanki¹, I. Rüedi¹, M. Bianda², and M. Steffen³

¹ Institute of Astronomy, ETH, CH-8092 Zürich, Switzerland

² IRSOL, Via Patocchi, CH-6605 Locarno-Monti, Switzerland

³ Institut für Astronomie und Astrophysik, Universität Kiel, D-24098 Kiel, Germany

Received 12 April 1995 / Accepted 26 August 1995

Abstract. We investigate the spectral signature of a hydrodynamic simulation of solar granulation and compare it with high resolution observations. The model gives the correct qualitative trend of increasing line width with decreasing continuum intensity seen by Nesis et al. (1992) and interpreted by them as a sign of post-shock turbulence. We find, however, that the profiles in the dark downflow lanes are broader even when there is no horizontal transonic flow or shock in the vicinity. We conclude that the observations of Nesis et al. do not provide any firm evidence for the presence of granular transonic flows.

Nevertheless, the simulation predicts a promising diagnostic of shocked horizontal flows. We find that at the locations of the shocks the line profiles are particularly broad, especially near the solar limb. We present observations of quiet solar regions that show this specific signature of shocks and thus support the theoretical prediction of transonic granular flows.

Key words: convection – Sun: granulation – line: profiles – hydrodynamics – shocks

1. Introduction

Simulations of convection under roughly solar conditions, in particular with low viscosity, show horizontal flows well in excess of the local sound speed (Cattaneo et al. 1989, 1990; Malagoli et al. 1990; Steffen 1991; Steffen & Freytag 1991; supersonic flows are also present in the simulations of Nordlund & Stein 1989, see Rast et al. 1993). Recently Nesis et al. (1992) presented circumstantial observational evidence for such flows in high spatial resolution spectrograms of the Ni I line at 4912 Å, namely on excess width of the line profile in dark intergranular lanes relative to the bright granule centres. An excess width of similar magnitude had earlier been observed by Holweger & Kneer (1989). Nesis et al. (1992) argue that this excess width, on average 10–15 mÅ, is due to increased turbulence in the dark lanes introduced by the shocks that brake the transonic flows back into the subsonic regime. Nevertheless, Nesis et al. (1992) did, in their final paragraph, point out that other interpretations of their observations cannot be ruled out.

In the present paper we first test a hydrodynamical simulation of granular convection by comparing parameters of synthetic line profiles with the values observed by Nesis et al. (1992). The simulation was especially designed to represent the Sun, in that it was carried out for solar effective temperature and opacity and is based on a realistic equation of state and a detailed description of radiative transfer.¹ This approach also allows us to investigate the diagnostic of transonic flow proposed by Nesis et al. (1992) within the context of a 2-D granular simulation.

Later we distil another observational diagnostic of supersonic shocked flows from the hydrodynamic simulations and compare it with observations obtained at the Istituto Ricerche Solari Locarno (IRSOL).

2. Hydrodynamic models

The model used by us, the 2-D simulation of Steffen (1991) and Steffen & Freytag (1991), has previously been demonstrated to reproduce many aspects of spatially resolved and averaged observations of solar spectral lines. Here we confront it with two sets of high spatial resolution observations. The hydrodynamic model has been amply documented elsewhere (e.g. Steffen et al. 1989) and we restrict ourselves to pointing out those properties that are of greatest relevance to the present investigation.

The simulation is carried out on a 2D Cartesian grid with 142 (horizontal) × 61 (vertical) mesh points. In the horizontal direction periodic boundary conditions are adopted, resulting in a repetition of the flow pattern with a period of 5250 km, large enough to accommodate several ‘granules’ side by side within the computational box. In the vertical direction the model extends from about 700 km below the visible surface (defined by $\tau_R = 1$, where τ_R is the Rosseland mean opacity) up to the temperature minimum near 500 km above $\tau_R = 1$, spanning a total of more than 6 pressure scale heights. The bottom boundary condition is designed to allow a free flow of gas out of and into the computational domain, keeping the total mass within the

¹ Note, however, that a 2-D simulation cannot contain a 3-D phenomenon, such as turbulence.

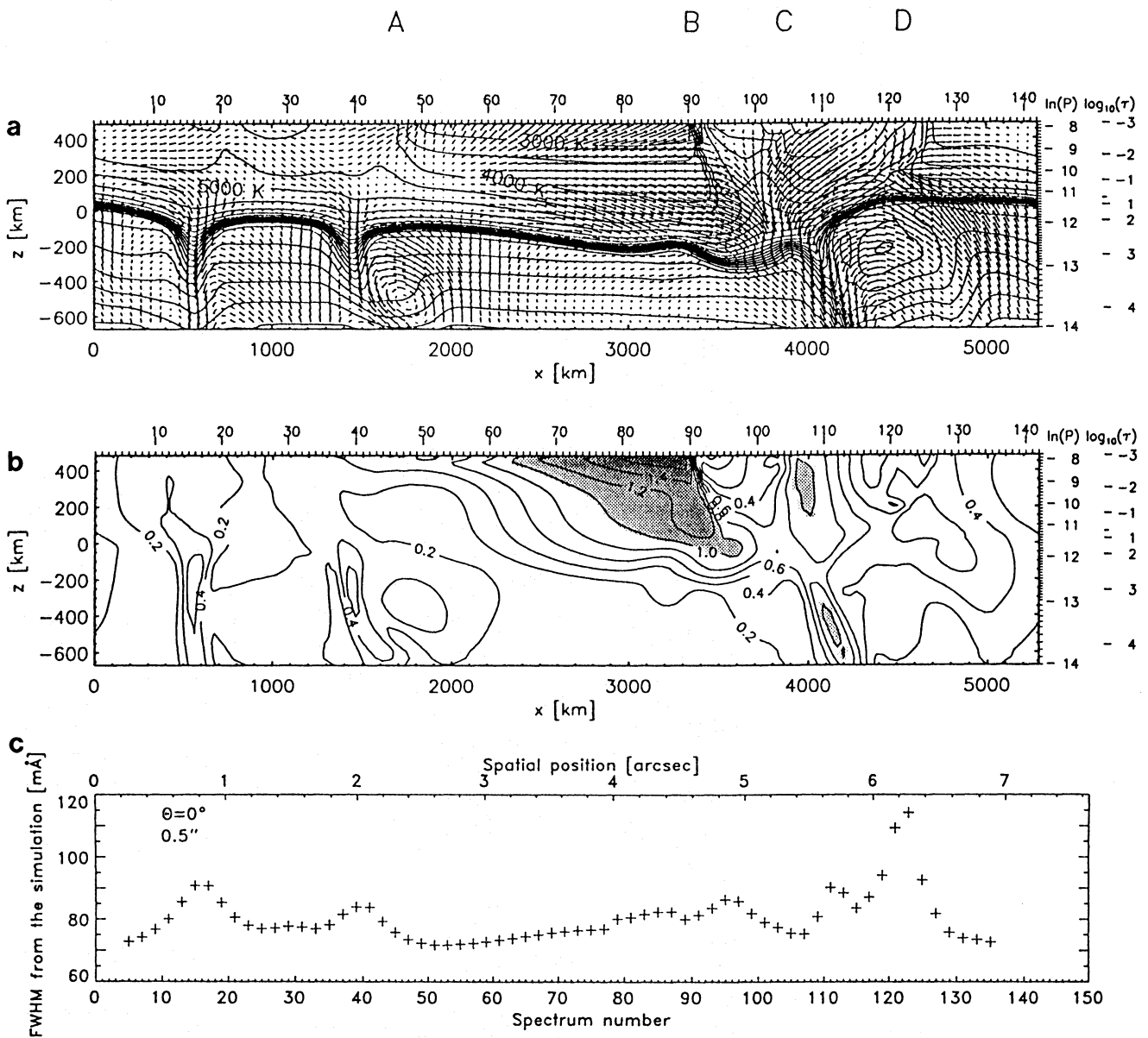


Fig. 1a–c. Representative snapshot from a numerical simulation of granular convection at the solar surface ($T_{\text{eff}} = 5770$ K, $\log g = 4.44$). The model is computed in 2D Cartesian geometry on a 142×61 grid (indicated by small tick marks at the top and at the right hand side of the box), adopting periodic boundary conditions in the horizontal direction with a period of 5250 km. Open boundary conditions are designed to minimize artificial disturbances of the flow at bottom and top. The computational domain comprises the photosphere and the uppermost layers of the solar convection zone. **a** The velocity field is indicated by curved arrows (pseudo streamlines integrated over 15 s); maximum velocity amounts to 10 km/s at this instant. Contour lines in steps of 500 K indicate the temperature structure; maximum temperature is 13 700 K. The two columns at right show the natural logarithm of the mean gas pressure [dyn cm^{-2}] and the logarithm of the mean Rosseland optical depth, $\bar{\tau}_R$. The zero point of the height scale at left corresponds to the layer with $\bar{\tau}_R = 1$. Letters A to D mark the locations of strong horizontal velocity gradients (see text). **b** For the same instant, contour lines indicating the Mach number, M , of the flow are plotted ($M = \sqrt{(u_x^2 + u_z^2)}/c_s$). In shaded areas the flow is supersonic. **c** Full width at half minimum (FWHM) vs. spatial position resulting from this snapshot when viewed vertically (i.e. at $\mu = \cos \theta = 1$). Here θ is the heliocentric angle. The calculated spectra have been smeared to correspond to a spatial resolution of $0.6''$

model constant. The top boundary is also open, permitting a (partial) transmission of pressure waves.

The foundation of this simulation are the time-dependent, non-linear basic equations of hydrodynamics (conservation of mass, momentum and energy), which are integrated numerically. The numerical method adopted for this purpose is essentially the bicharacteristics method described in some detail by Stefanik et al. (1984). The most important feature of the present model calculation is undoubtedly the incorporation of a realistic energy equation, accounting for the energy exchange by non-local, multi-dimensional, frequency-dependent radiative transfer, which is a prerequisite for the calculation of a realistic photospheric temperature structure and synthetic line profiles. The method for computing the radiation field, which is based on the solution of the equation of radiative transfer on a system of several thousand rays, is valid under optically thick and optically thin conditions as well as in the thin boundary layer around $\tau_R = 1$. The equation of state includes ionization of H, He I, He II and the formation, excitation and dissociation of H_2 molecules.

Turbulence on subgrid scales is modeled using the concept of subgrid scale (SGS) eddy viscosity (cf. Deardorff 1970, 1971). This approach limits the grid Reynolds number to ≈ 1 . However, the SGS viscosity is not sufficient to stabilize shock fronts. In the present case this is achieved by introducing a monotonic interpolation scheme (Steffen, 1990) into the bicharacteristics scheme. This allows the modeling of very steep gradients (shock fronts), but locally reduces somewhat the accuracy of the solution, which may lead to errors in e.g. the shock propagation speed. While the calculated shock structure may also be affected by such errors, the derived shock properties should be at least qualitatively correct.

Isotherms and velocity arrows of a snapshot of the dynamic, rapidly changing model are plotted in Fig. 1a. Isocontours of the Mach number are plotted in Fig. 1b.² The flows in the shaded regions are supersonic. Supersonic velocities in the visible layers are mainly horizontal, running towards the right in the central part of the model in this snapshot. A more inclined, less extended supersonic flow is present around point C. Locations of strong (mainly horizontal) velocity gradients are marked by A, B, C and D. Points B and C are associated with supersonic flows, while the Mach number exceeds 0.6 at point B and 0.4 at D. A fully developed shock is present at point B. Note that the thermal effects of this shock are concentrated in the upper photosphere and that the abrupt braking takes place over a single grid point. Due to the strong cooling by the adiabatic expansion of the supersonic gas upstream of the shock at B, very large Mach numbers are present near the upper boundary of the simulation between horizontal grid points 70 and 90.

Horizontal velocities dominate the photosphere, while vertical velocities are predominant in the subsurface layers. The largest vertical velocities are almost exclusively downflows (cf. Nordlund & Stein 1989). They are associated with cool material, small temperature gradients and large vertical velocity gradients

(the downflow velocity increases with depth at and just below the surface). Downflows are present in the snapshot plotted in Fig. 1a at grid points 16, 40 and 110.

3. Line calculations

The Ni I 4912.03 Å line is a Landé $g = 0$ line, with excitation potential $\chi_e = 3.77$ eV, average equivalent width $W_\lambda = 53$ mÅ in the quiet Sun and logarithmic oscillator strength $\log gf = -0.87$ (Thévenin 1989). We synthesize the line using the same radiative transfer code as Solanki et al. (1992), cf. Solanki (1987). The calculations are in LTE. The employed Diagonal Element Lambda Operator technique (DELO, Rees et al. 1989, cf. Murphy 1990) gives stable results, even along rays that cross the shock.

We first calculate the Ni I line using the average quiet-Sun model of Maltby et al. (1986) and we compare it with a disk-centre quiet-Sun Fourier transform spectrum (see Solanki 1987 for a description of the data) to fine-tune parameters like the $\log gf\epsilon$ value and the fudge-factor to the Van der Waals damping constant (ϵ is the nickel abundance).

Next we calculate the line along (vertical or inclined) rays passing through the hydrodynamic simulation. The rays are separated by the horizontal grid-point separation of the model. We interpolate the relevant atmospheric quantities onto the ray linearly from the 4 corners of a rectangular grid cell, taking care that the sampling of the optical depth scale along the ray is dense and equally spaced.

When comparing with the observations we spatially smear the synthetic spectrum by replacing the profile calculated for a given horizontal grid point by a weighted sum of neighbouring profiles (see Sect. 5).

4. Observations

We compare the synthetic profiles with two sets of data. The high-resolution disk centre spectra described by Nesis et al. (1992), in particular the published correlation between line width and continuum intensity, form the first set.

The second and main data set we consider is composed of spectra obtained at IRSOL in Locarno, Switzerland, with the refurbished 45 cm Gregory telescope and spectrograph. We mainly discuss the three CCD spectra obtained in the quiet Sun at $\mu = 0.55$ (towards the north solar pole) having the highest spatial resolution out of a larger set of spectra. The spatial extent of each spectrum is $73''$, the pixel size is $0.18''$ in the spatial and 3.5 mÅ in the spectral direction. The spectral resolving power and spectral range are 330 000 and 4911–4913 Å, respectively. The exposure time was 0.5 s.

Fig. 2 shows from top to bottom the continuum intensity, line depth, equivalent width W_λ , full width at half minimum (FWHM) and relative wavelength shift $\Delta\lambda$ of Ni I 4912 Å along the spectrograph slit for one of these frames.³ Note in

² Fig. 1c will be discussed in Sect. 6.1 and is only plotted here to facilitate comparison with the hydrodynamic model.

³ To prevent contamination by blends the contribution of the line wings to the equivalent width was neglected.

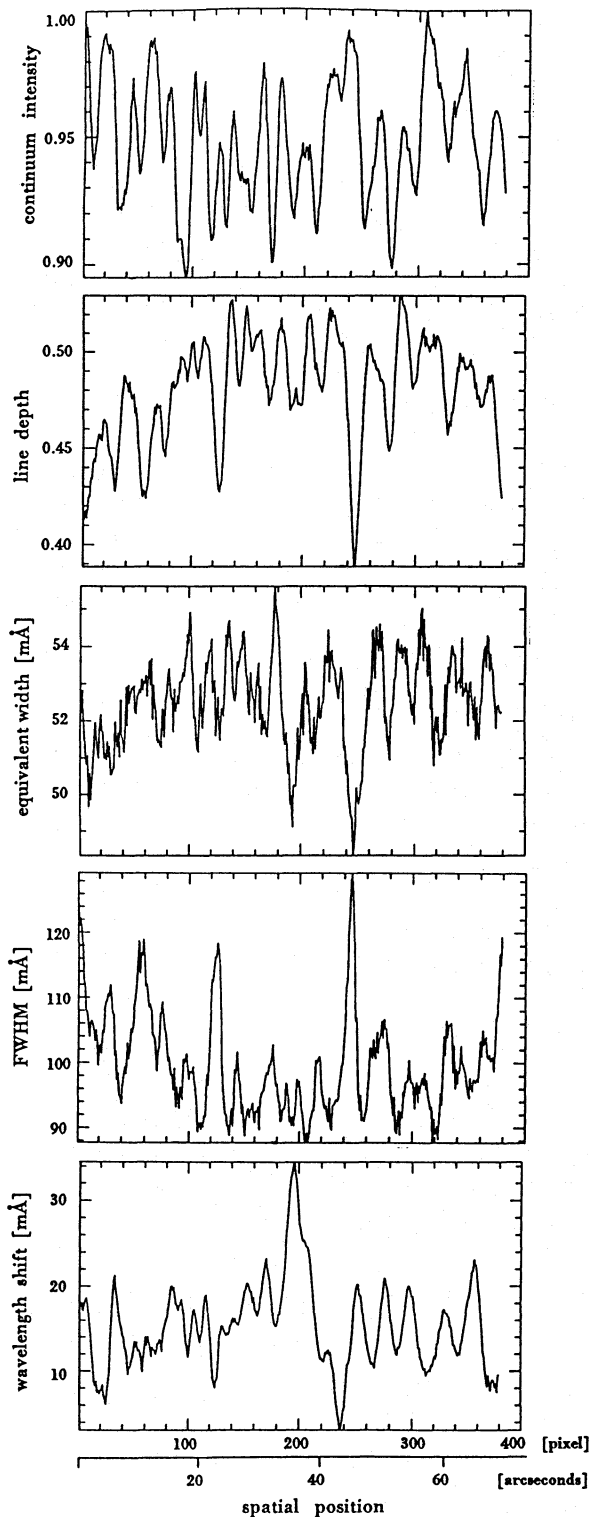


Fig. 2. From top to bottom: Normalized continuum intensity I_c , line depth d , equivalent width W_λ , FWHM and relative wavelength shift $\Delta\lambda$ of observed Ni I profiles vs. spatial location along slit. Observations made at IRSOL near the solar limb: $\mu \approx 0.5$. Positive wavelength shifts correspond to flows away from the observer

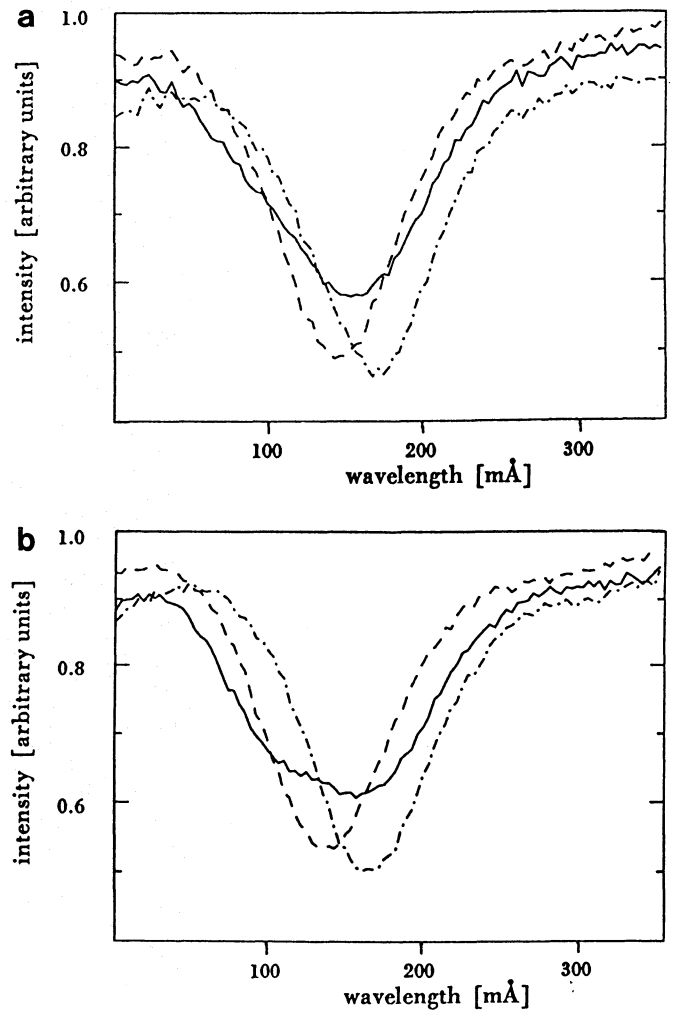


Fig. 3a and b. Examples of profiles from two different CCD frames. For each frame a typical granular profile (bright continuum, blueshifted line: dashed), a typical intergranular (dark continuum, redshifted line: dot-dashed) and an anomalously wide profile (solid) are plotted. The broad profile plotted in **a** corresponds to pixel No. 250 in Fig. 2

particular the large excursions in FWHM near pixels 60, 130 and 250. These pixels also show anomalies in the line depth and wavelength shift, but are comparatively unremarkable in continuum intensity and equivalent width. The relative change of the equivalent width is less than one fourth that of the FWHM. The dramatic increase in line width (by 20–35% relative to the background value in this observation) is compensated by the decrease in line depth to leave the equivalent width relatively unchanged.

Such features were only seen in the spectra obtained under the best seeing conditions. The excessive line widths, the small, if any, decrease in equivalent width, the greater number closer to the limb and the tendency to be blueshifted all suggest that this phenomenon is not magnetically related, although simultaneous polarimetric observations were not obtained and would be useful. Two examples of exceptionally broad profiles are plotted in Figs. 3a and 3b (solid curves) together with typical examples

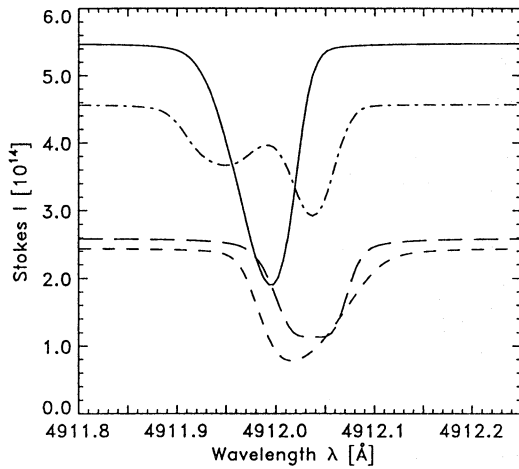


Fig. 4. Four spatially unsmeared synthetic Ni I 4912Å profiles calculated at different horizontal spatial positions in the 2-D simulation at $\mu = 1$ (vertical rays). Solid profile: spatial position 128 in Fig. 1a, dot-dashed profile: spatial position 123 (i.e. both near point D), long dashes: spatial position 95, short dashes: spatial position 16

of profiles from bright upflowing granules (dashed) and dark downflowing intergranular lanes (dot-dashed). The solid profile in Fig. 3a corresponds to pixel 250 of the same frame illustrated in Fig. 2, while Fig. 3b shows an anomalous profile taken from another CCD frame. The FWHM of the solid profile in Fig. 3b is more than a factor of 1.5 larger than the average value.

5. Results

5.1. Disk centre

Profiles synthesized along individual rays show little correspondence with the observations of Nesis et al. (1992) or Holweger & Kneer (1989). The synthetic profiles have a very wide variety of shapes, strengths, continuum intensities, widths and shifts. In Fig. 4 a set of selected unnormalized, unsmeared profiles produced along vertical rays passing through the 2-D model are plotted to illustrate the range of line profile shapes produced by it. They correspond to a spatial resolution of $0.1''$. By spatially smearing the profiles to simulate the influence of seeing, i.e. by forming weighted means over neighbouring profiles, the correspondence with the observations is substantially increased. We have chosen a Gaussian smearing function. The amount of smearing is determined by comparing the ratio between the continuum intensities of the smeared profiles in the up- and downflowing parts of the model with the ratio seen in Fig. 1 of Nesis et al. (1992). In the following we concentrate on the appropriately spatially smeared profiles.

We find that the hydrodynamic model gives the correct qualitative behaviour, i.e. line profiles arising in the dark downflow lanes are broader than those formed in the bright upflowing part of the atmosphere, with the exception of one narrow spatial range at which the profiles have up to 1.5 times the average width. For the moment we neglect these ‘anomalous’ profiles. The FWHM of the smeared synthetic profiles are plotted vs. the

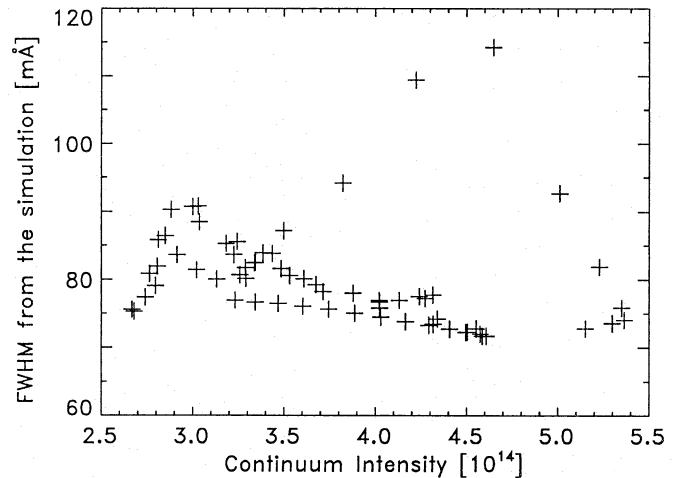


Fig. 5. The FWHM of the Ni I 4912Å line vs. continuum intensity at solar disk centre, i.e. at $\mu = \cos \theta = 1$, synthesized from the hydrodynamic simulation

continuum intensity I_c in Fig. 5. This figure should be compared with Figs. 2a and b of Nesis et al. (1992). The equivalent width of the line also tends to decrease slightly with increasing continuum intensity, but much less strongly than the FWHM. This relative insensitivity is also in agreement with the observations.

The line width as a function of spatial position is shown in Fig. 1c. It can be compared directly with the velocity arrows and isotherms of the model in Fig. 1a and with the Mach number in Fig. 1b. The large anomaly in line-width around grid point 123 is produced at a location at which an upflow from below meets a downflow from above. Note the increase in line width above the downflow lanes (at horizontal grid points = spectrum numbers 16, 40, 110). In particular the significant excess broadening around spatial positions 16 and 40 are quite unrelated to any transonic flows in the observable layers, since all velocities in their vicinity are subsonic. Therefore, our simulations provide an alternative explanation to the observations of Nesis et al. (1992), who interpreted them in terms of post-shock turbulence. We conclude that any enhanced line widths seen at disk centre within intergranular lanes need not be the result of nearby shocks, but probably reflect the physical structure of the downflow lanes themselves. The shocks do show enhanced FWHM, but are not usually correlated with cool gas (e.g. spatial position 95). The observations of Nesis et al. (1993) that broadened lines are found at the boundary between granules and intergranular lanes are closer to our model predictions of the signature of shocked gas.

Since no turbulent velocity was used when synthesizing the line profiles, we must identify other sources of the excess broadening in the downflow lanes. The two simplest possibilities that come to mind are 1) different velocity gradients in the bright and dark parts of the granules, and 2) different temperature gradients.

Consider the first mechanism. Both vertical and horizontal gradients of the vertical velocity can produce the desired effect.

In the hydrodynamic simulations the vertical velocity gradient is generally larger in the dark lanes than in the brighter upflows.

Horizontal gradients of the vertical velocity play a substantial role in producing the line width difference because the dark lanes are usually narrower than the bright granules. Consequently, when averaging over multiple rays (to simulate seeing) we average over a larger spread of Doppler shifts in the dark areas than in the bright ones. This helps broaden the smeared profiles from the dark lanes relative to those from the bright granule centres.

The second proposed mechanism (temperature gradients) may play a role because, although the Ni I line is not particularly strong, it is not completely unsaturated. We have tested and confirmed the potential of this mechanism for influencing the FWHM with the help of simple 1-D hydrostatic atmospheres with different effective temperatures and different $dT/d\tau$. Note that in the simulations $dT/d\tau$ is generally smaller along rays passing through the dark lanes than along rays through the bright granule centres, which suggests that temperature gradients probably help in producing the observed effect: Small $dT/d\tau$ lead to less deep, broader profiles than steeper temperature gradients. Note, however, that in general just changing the temperature gradient also significantly affects the equivalent width of the line profiles, so that we do not consider this to be the dominant mechanism producing broader profiles in the intergranular lanes.

5.2. Limb

Fig. 6 shows, from top to bottom, continuum intensity, line depth, W_λ , FWHM and $\Delta\lambda$ obtained from the simulation at a heliocentric angle of 55° (i.e. looking from top left to bottom right in the snapshot shown in Fig. 1a). The simulated spectra have been smeared to correspond to a spatial resolution of roughly $0.5''$, which corresponds to 630 km on the solar surface at $\theta = 55^\circ$.

The dominant feature of the figure is the anomaly in the line width near spectrum No. 85, which corresponds to point B in Fig. 1, i.e. the strong horizontal shock (the spectrum numbers refer to the horizontal position at which the central ray of the bundle enters the top of the model and need not correspond exactly to the spatial location of the feature in Fig. 1a due to the inclined line of sight). The large line width is produced by the large velocity gradient across the shock, and is modified somewhat by the spatial smearing.⁴ The line depth is also strongly decreased at this location (probably due to the shock induced heating in the upper photosphere), while equivalent width and continuum intensity are not so strongly affected. In contrast, the downflow lanes do not show any significant line broadening at this viewing angle, a major advantage of observing near the limb when searching for granular shocks.

When comparing with the IRSOL observations we find that there is considerable similarity between the properties of the simulated and the observed line profiles with anomalously large

⁴ The broadest profiles often show two minima, due to gas in the up- and downstream parts of the shocks.

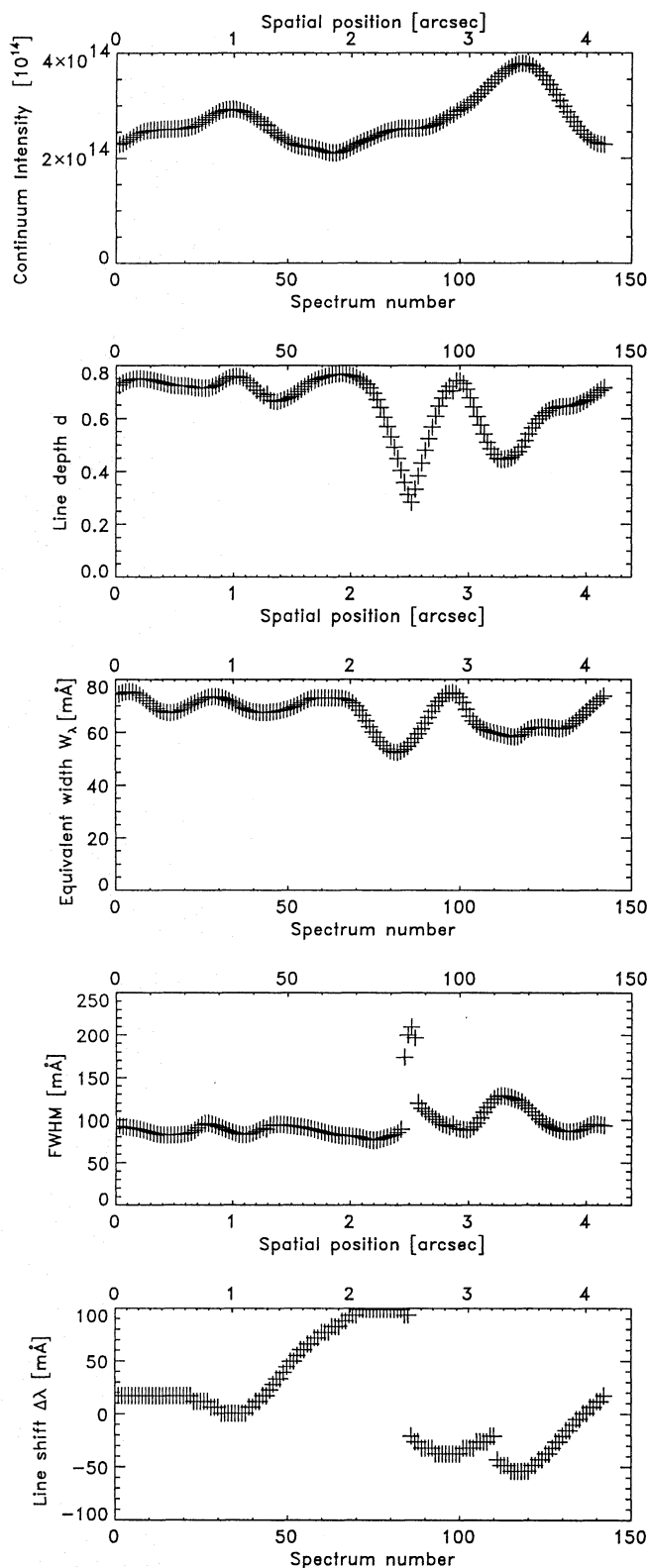


Fig. 6. From top to bottom: Simulated I_c , d , W_λ , FWHM and $\Delta\lambda$ vs. spatial location. All values have been derived after spatially smearing the profiles to correspond to a spatial resolution of $0.5''$. $\theta = 55^\circ$, i.e. $\mu = 0.57$

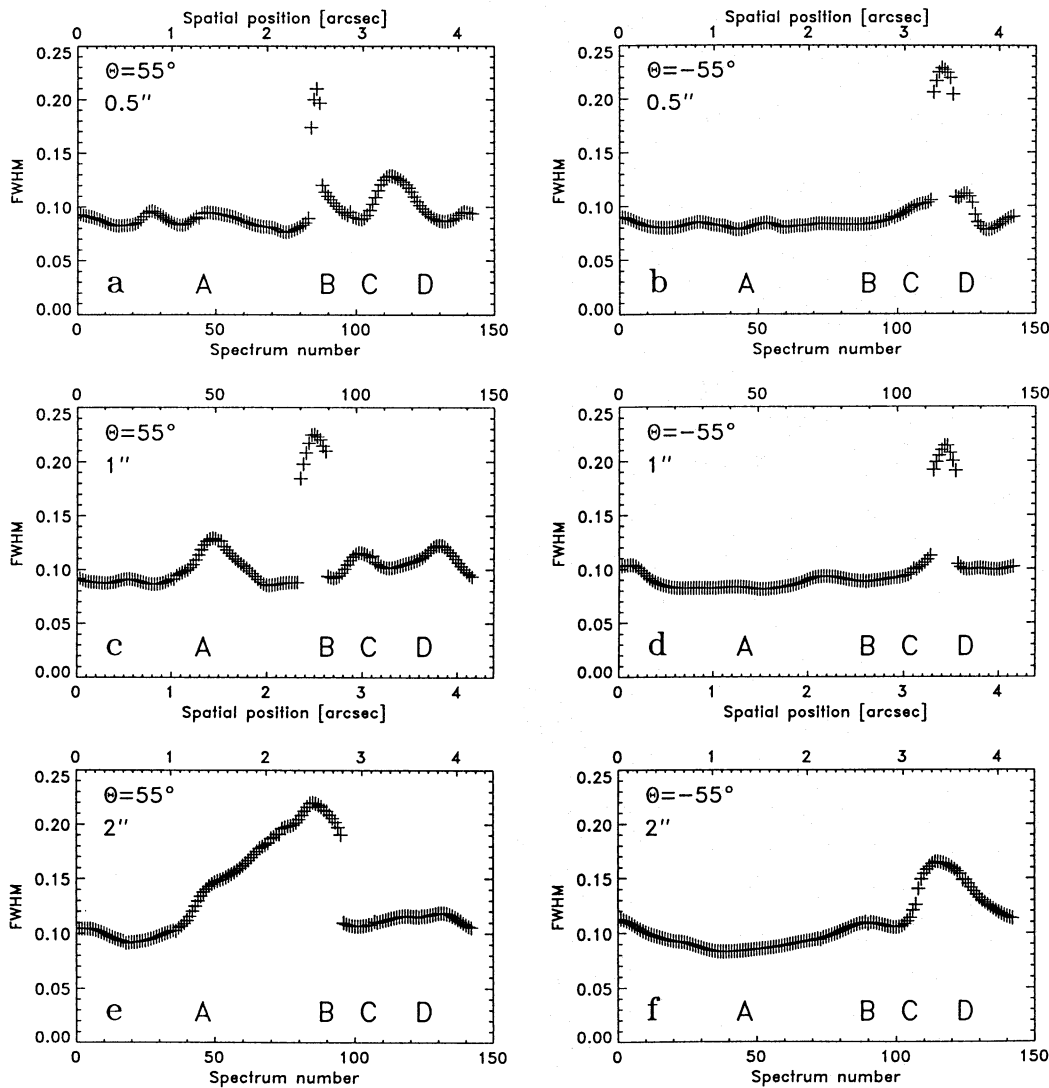


Fig. 7a–f. FWHM of synthetic profiles vs. spatial location. **a** and **b**: Simulated spatial resolution of $0.5''$, **c** and **d**: $1''$, **e** and **f**: $2''$. Left hand panels: $\theta = +55^\circ$, right hand panels: $\theta = -55^\circ$. The letters A–D correspond to the features designated by the same letters in Fig. 1

widths, although the anomaly in FWHM is larger in the simulations than in the observations. (Note the difference in spatial scale between Fig. 6, whose total width is only $\approx 4.5''$, and Fig. 2 with a total width $\approx 70''$.) This similarity suggests that we are observing the signature of granular shocks.

One discrepancy to the observations is that the simulations show a jump in velocity (line shift) at the spatial location of the shock. This is an artifact produced by the fact that the anomalous profiles often show two minima, one each due to the gas in the up- and downstream parts of the shock. The wavelength of each minimum remains stable, but their relative depths change across the shock. The jump in $\Delta\lambda$ is produced at the location at which both minima are equally deep. At lower spatial resolution the two minima merge and the jump disappears. This is also expected to happen at other viewing angles (e.g. when observing a shock obliquely in a 3-D situation).

The spatial resolution turns out to be a key factor for the behaviour of other line parameters as well, in particular for the

line width. Fig. 7 illustrates this. In Fig. 7a we plot the FWHM of Ni I 4912Å across the hydrodynamic simulation at $\theta = +55^\circ$ (looking from left to right), while Fig. 7b shows the same for $\theta = -55^\circ$ (i.e. looking from right to left). Peaks are marked by letters showing the corresponding features in the hydrodynamic simulations in Fig. 1a. In Figs. 7c and d, we show the same quantities, but now for a spatial smearing corresponding to $1''$. Finally, a spatial resolution of $2''$ is simulated in Figs. 7e and f. The broadest profiles can all be identified with regions with large horizontal velocity gradients associated with supersonic flows. The converse is not true: Not all gradients of supersonic velocities show up as ultrabroad profiles. A particularly striking example is the strong shock at point B, which does not show up in the FWHM when observed at -55° . At lower resolution the peaks in the FWHM tend to broaden. In addition, more than one such location can contribute to a given spatially smeared line profile, causing, e.g., the spatially very extended peak in Fig. 7e and leading to an increased average FWHM (note that

the averaged FWHM is in general not equal to the FWHM of the averaged profile). Our simulations suggest that the signature of shocks is most undiluted and straightforward at the highest spatial resolutions, calling for higher spatial resolution observations. Nevertheless, even at $2''$ all increases of the FWHM by factors greater than approximately 1.3 are associated with supersonic flows. For comparison, we estimate the spatial resolution of the best IRSOL observation to be approximately $1''$ (from a comparison of the continuum contrast with smeared simulations).

The dependence of the FWHM on viewing angle ($\theta = \pm 55^\circ$ in this case) is mainly due to the fact that the high velocities are not exactly horizontal, but rather somewhat inclined. This illustrates not only the importance of the viewing angle, but also of bearing in mind that in the 3-D Sun shocks will rarely be viewed head-on, so that their signature should be correspondingly weaker than in 2-D simulations, bringing the synthesized observations more into line with the actual observations.

6. Discussion and conclusions

We have investigated the spectroscopic properties of a 2-D hydrodynamic model of solar granulation. First we analysed at solar disk centre the FWHM and W_λ of a Ni I line as a function of continuum intensity I_c . The calculations are compared with the high resolution observations of Nesis et al. (1992), who interpreted the increased FWHM they observed in the dark intergranular lanes mainly in terms of increased turbulence produced by shocks and thus as evidence for transonic flows. Whether turbulence is or is not the cause of non-thermal line broadenings has been the subject of considerable debate in the past (e.g. Olson 1966, Gail et al. 1976, Nordlund 1980, Holweger & Kneer 1989) and the matter must still be considered to be unresolved.

The model qualitatively reproduces the observed dependence of FWHM on I_c . Differences in velocity and temperature gradients in the bright and dark areas are responsible for this difference between the FWHM of the synthetic profiles of the upflowing and downflowing parts.

Our simulations, however, show that the line FWHM is increased in downflows, even far from transonic flows or shocks. This suggests that the increased FWHM in the cool downflow lanes is due to the local properties of the downflow lanes and is not related to transonic flows. Thus, although observations such as those of Holweger & Kneer (1989) and Nesis et al. (1992) are valuable for testing models of granular convection, they do not constitute unambiguous evidence for transonic flows in solar granulation. The excess line widths observed more recently at the boundary between granules and intergranular lanes by Nesis et al. (1993) may, however, in the context of our simulations, reflect shocks.

Since transonic velocities in visible atmospheric layers are mainly horizontal in the simulations, observations near the limb should be better suited to detect them. Consequently, we have recorded spectra of solar granulation and also calculated synthetic profiles closer to the limb of the Sun. Both observations and simulations show ultrabroad line profiles confined to within

small regions on the solar surface. The simulations show that such ultrabroad profiles near the limb are produced at locations at which the horizontal velocity and its gradient are large. In particular such profiles are located in regions having nearly horizontal supersonic (or close to supersonic) flows in the mid or upper photosphere, and may be associated with shocks. Spectra obtained at a spatial resolution of roughly $1''$ show at some locations a sufficient similarity to these synthetic spectra to warrant a tentative identification with supersonic and possibly shocked granular flows, although further modelling and in particular higher spatial resolution observations related to granular shocks would be extremely useful (since the signature of the shocks is clearest at the highest spatial resolution).

Further indirect evidence for supersonic flows in the upper photosphere and lower chromosphere may be provided by the widths of CO fundamental band lines seen in emission beyond the solar limb (Solanki et al. 1994).

Acknowledgements. We thank K.H. Duensing, G. Küveler and E. Wiehr for their help and dedication, which has enabled refurbishment of the Locarno telescope with financial support from the Canton of Ticino and the city of Locarno.

References

- Cattaneo F., Hurlburt N.E., Toomre J., 1989, in *Solar and Stellar Granulation*, R.J. Rutten and G. Severino (Eds.), Reidel, Dordrecht, p 415
- Cattaneo F., Hurlburt N.E., Toomre J., 1990, *ApJ* 349, L63
- Deardorff J.W. 1970, *J. Fluid Mech.* 41, 453
- Deardorff J.W. 1971, *J. Comput. Phys.* 7, 120
- Gail H.-P., Sedlmayr E., Traving G., 1976, *A&A* 46, 441
- Holweger H., Kneer F., 1989, in *Solar and Stellar Granulation*, R.J. Rutten, G. Severino (Eds.), Kluwer, Dordrecht, p. 173
- Malagoli A., Cattaneo F., Brummell N.H., 1990, *ApJ* 361, L33
- Maltby P., Avrett E.H., Carlsson M., Kjeldseth-Moe O., Kurucz R.L., Loeser R., 1986, *ApJ* 306, 284
- Murphy G.A., 1990, NCAR Cooperative Thesis No. 124
- Nesis A., Bogdan T.J., Cattaneo F. et al., 1992, *ApJ* 399, L99
- Nesis A., Hanslmeier A., Hammer R. et al., 1993, *A&A* 279, 599
- Nordlund Å., 1980 in *Stellar Turbulence*, D.F. Gray, J.L. Linsky (Eds.), Springer, Berlin, p. 213
- Nordlund Å., Stein R.F., 1989, in *Solar and Stellar Granulation*, R.J. Rutten, G. Severino (Eds.), Kluwer, Dordrecht, p. 453
- Olson E.C., 1966, *ApJ* 143,904
- Rast M.P., Nordlund Å., Stein R.F., Toomre J., 1993, *ApJ* 408, L53
- Rees D.E., Murphy G.A., Durrant C.J., 1989, *ApJ* 339, 1093
- Solanki S.K., 1987, Ph.D. Thesis, No. 8309, ETH, Zürich
- Solanki S.K., Rüedi I., Livingston W., 1992, *A&A* 263, 312
- Solanki S.K., Livingston W., Ayres T., 1994, *Science* 263, 64
- Stefanik R.P., Ulmschneider P., Hammer R., Durrant C.J. 1984, *A&A* 134, 77
- Steffen M. 1990, *A&A* 239, 443
- Steffen M., 1991, in *Stellar Atmospheres: Beyond Classical Models*, L. Crivellari, I. Hubeny, D.G. Hummer (Eds.), Kluwer, Dordrecht, p. 247
- Steffen M., Freytag B., 1991, *Reviews of Modern Astron.* 4, 43
- Steffen M., Ludwig H.-G., Krüß A., 1989, *A&A* 213, 371
- Thévenin F., 1989, *A&AS* 77, 137